[Short title + Author Name - P&H title] 17 (2024) 105647

Contents lists available at ScienceDirect

Arabian Journal of Chemistry

journal homepage: www.ksu.edu.sa

Original article

Novel synthesis and characterization of magnesium-doped $CoFe_2O_4$ nanoparticles –SiO_2 –3-aminopropylethoxysilane– gallic acid magnetic nanocomposite for effective removal of cationic dyes

Shameran Jamal Salih *, Layth Imad Abd Ali, Wali Mahmood Hamad

Department of Chemistry, Faculty of Science and Health, Koya University, Koya KOY45, Kurdistan Region – F.R., Iraq

ARTICLE INFO

Novel synthesis and characterization of magnesium-doped $CoFe_2O_4$ nanoparticles

Keywords:
Magnetic nanocomposite
Dye's removal
Methylene blue
Rhodamine B
Adsorption capacity
Water treatment

ABSTRACT

Magnesium-doped CoFe2O4 nanoparticles (MgCF)@SiO_2-NH-COOH were prepared through a step-wise procedure for the removal of two cationic dyes from real wastewater. MgCF was successfully synthesized through the co-precipitation technique. Subsequently, these nanoparticles were coated within a silica (SiO2) shell and functionalized with amino groups utilizing 3-Aminopropylethoxysilane (APTES). To assess its adsorption capabilities, the nanocomposite underwent further modification with Gallic acid (GA). MgCF@SiO_2-NH-COOH has a well-developed pore structure with a BET surface area of 31.655m^2/g, which also has a crystalline structure. Adsorption tests revealed the excellent performance of MgCF@SiO_2-NH-COOH in removing Methylene Blue (MB) and Rhodamine B (RhB) dyes. Kinetic studies demonstrated that the adsorption of MB and RhB followed the Boyd kinetic model. The Langmuir isotherm model provided the best fit for the experimental data, with a maximum adsorption capacity of 103 mg/g and 89 mg/g for MB and RhB, respectively. Moreover, recycling tests established the high stability and reusability of MgCF-SiO_2-APTES-GA nanocomposites, with consistent adsorption performance over at least five cycles. At the first stage, the adsorption was 98.6 % for MB and 95.3 % for RhB, and after five regenerations, the adsorption was 82.5 % for MB and 79.6 % for RhB. This research offers a cost-effective compound that addresses pressing environmental concerns related to the removal of organic dyes from wastewater.

1. Introduction

In the past few decades, magnetic nanoparticles (MNPs) have demonstrated significant potential in various applications due to their unique material properties (Iqbal et al., 2023). The high surface area, low toxicity, high activity, thermal stability, and feasibility of surface functionalization make MNPs attractive. Among MNPs, ferrite materials with the general formula MFe_2O_4 have attracted attention due to their superparamagnetic behavior which can be finely tuned by substituting different M^{2+} cations, resulting a wide range of magnetic properties (Salih and Mahmood, 2023).

One of the most prominent and extensively investigated groups of magnetic nanoparticles is cobalt ferrite ($CoFe_2O_4$). It possesses specific chemical, physical, electrical, mechanical, and physicochemical features, including a wide range of redox states, excellent permeability and chemical stability, superior electrochemical stability, mechanical hardness, wear resistance, ease of synthesis, electrical insulation, a high Curie temperature and coercivity, a moderate saturation magnetization, and a high anisotropy constant (Ali et al., 2020). These outstanding qualities have several applications in various sectors especially in wastewater treatment.

The presence of dyes and other pollutants in water bodies has been a concerning issue. The total annual production of commercial dyes from various industries is estimated at around 700,000 tons (Salih et al., 2022). Removing these dyes presents a significant challenge due to their diverse synthetic origins. The significant considerable volume of dye residue discharged into aquatic environments poses a grave threat in terms of toxicity, can potentially resulting in death for all living organisms. Therefore, it is essential to minimize their concentration to permissible levels before releasing them into the environment.

Methylene Blue (MB) and Rhodamine B (RhB) are common cationic dyes employed in the textile, dyeing, and printing industries. These dyes possess diverse chemical structures with substituted aromatic groups and are positively charged. They belong to the category of basic dye that

---

* Corresponding author.
E-mail address: shameran.jamal@koyauniversity.org (S.J. Salih).

https://doi.org/10.1016/j.arabjc.2024.105647
Received 11 November 2023; Accepted 22 January 2024

readily dissolves in water, producing colorful ions upon dissolution. Furthermore, these dyes have the potential to trigger allergic reactions and can undergo metabolic processes leading to the formation of carcinogenic byproducts (Akpomie et al., 2023).

$CoFe_2O_4$@Hydroxyapatite as a magnetic heterostructure has been synthesized to remove Congo Red dye. The adsorption capacity was reported as 15.25 mg/g (Dănilă et al., 2023). In another research, $CoFe_2O_4$@methylcellulose /activated carbon was synthesized for the removal of Reactive Red 198 (RR198) dye (Nasiri et al., 2022). The most significant features of this nano-magnetic adsorbent were the cheap cost of biodegradability, biocompatibility, and hydrophilicity.

Developing an efficient and cost-effective approach for the simultaneous removal of organic dyes presents a significant challenge. Various methods for wastewater treatment have been employed, including adsorption, natural degradation, and chemical oxidation. Biological degradation and chemical oxidation have some potential drawbacks including lack of selectivity**,** slow reaction rates, dependency on environmental factors, and high cost. On the other hand, adsorptive removal stands out as a cost-effective, highly efficient, and rapid approach to wastewater treatment. This method is less susceptible to the presence of toxic substances and is straightforward to implement (Li et al., 2023). In recent years, various materials such as agricultural residues, mesoporous silica, kaolin, gelatin fiber, and activated carbon have been used as adsorbents. However, despite their similarities, these materials face challenges in effectively separating aqueous solutions (Doan, 2023). To address the separation and preparation challenges mentioned earlier, metal ferrite nanoparticles emerge as a potential solution.

One of the critical features for nanoadsprbents is their biocompatibility. The importance of biocompatibility of nanoadsorbents for removing dyes lies in their ability to effectively remove dye pollutants from wastewater while minimizing potential negative impacts on the environment and human health. Therefore, in this study, we synthesize a biocompatible nanoadsorbent to remove dyes.

In the present study, we firstly synthesized magnesium-doped $CoFe_2O_4$ nanoparticles through a single step (co-precipitation) route. These MgCF nanoparticles were subsequently coated with silica (SiO_2) and functionalized with an amino group utilizing 3-Aminopropylethoxysilane (APTES). Afterward, the magnetite material underwent modification using Gallic acid (GA). It was then utilized to remove cationic dyes from natural wastewater.

2. Experimental

2.1. Chemicals and reagents

All materials that used in this work were of analytical grade and utilized without further purification. Cobalt chloride [$CoCl_2{\cdot}6H_2O$], ferric chloride [$FeCl_3{\cdot}6H_2O$], magnesium chloride [$MgCl_2{\cdot}6H_2O$], tetraethyl orthosilicate (TEOS), 3-Aminopropyl triethoxysilane (APTES) and Gallic acid were all purchased from Merck. Ammonium hydroxide (NH_4OH) (30 %) MB and Rhodamine B (RhB) were purchased from Sigma-Aldrich. The chemical structure of dyes is shown in Fig. S1.

2.2. Characterization

X-ray diffraction Philips PW1730 was used to determine the crystalline structure of the as-prepared nano-sorbents at room temperature. The magnetic characteristics of the nanocomposites under the impact of an applied magnetic field were recorded using an MDKB VSM at room temperature. The composition of the as-prepared nanocomposite was surveyed by recording infrared spectra over the range of 4000–400 cm^{-1} using an FTIR spectrophotometer (Thermo Avatar). The morphology of nanosorbents was analyzed using a specific FE-SEM system, the MIRA3 TESCAN. The particle size and morphology were characterized using TEM, the Philips CM120 TEM system. The BET model and N_2 adsorption method were used to determine the specific surface area, pore volume, and pore diameter using the BELSORP mini2 analyzer. Zeta potential measurements were carried out size and Zeta Potential Analyzer, Manufacturer: Brookhaven, model of 90 Plus PALS.

2.3. Preparation of magnesium-doped cobalt ferrite nanoparticles (MgCF)

Magnesium-doped cobalt ferrite (MgCF) nanoparticles were synthesized using co-precipitation method (Mund and Ahuja, 2017). Without the use of surfactants. Initially, stoichiometric amounts of $MgCl_2$, $CoCl_2$, and FeCl3 were introduced into the 50 ml of deionized water with precursor concentrations of Fe:Co:Mg (1:0.5:0.1). Next, the ammonia solution was dropped and dispersed into the solution until the pH reached approximately 10–12. The mixture was heated at 70–80 °C for 2 h with vigorous stirring. The resulting black precipitate was isolated using an external magnet and subjected to multiple rinses with deionized water to eliminate impurities, excess hydroxides, and unreacted salts. The final product was oven-dried at 105 °C overnight, annealed at 600 °C for 6 h, and stored for future applications. The schematic representation of the procedure for the synthesis of magnesium-doped cobalt ferrite NPs steps is shown in Fig. 1.

2.4. Coating of the first layer

The Stober process was employed to coat silica onto MgCF nanoparticles as the initial layer (Bektar et al., 2020, Khalid et al., 2023). Stober process is a technique based on the hydrolysis of tetraethylorthosilicate (TEOS) in the presence of NH_3 to produce a composite material known as MgCF@SiO_2. A mixture containing 10.2 ml of TEOS and 10.45 ml of ethanol was prepared and then subjected to sonication for approximately 15 min. Simultaneously, the nanoparticle solution was sonicated for 30 min and subsequently added to the first mixture of TEOS and ethanol. The resulting solution was stirred for 1 h and underwent gelation for several hours. Afterward, magnetic separation was used to isolate the particles, which were then washed three times with deionized water and finally oven-dried at 80 °C overnight.

2.5. Amino functionalization of MgCF@SiO_2 nanoparticles

To obtain amino functionalized MgCF@SiO_2 NPs using 3-aminopropyltriethoxysilane (APTES) the following steps were followed. Initially, 1 g of MgCF@SiO_2 was dispersed in a mixture of 150 ml ethanol/water (1:1) using probe sonication for 30 min. Subsequently, 6 ml of APTES was poured into the mixture. Then, the resulting solution was stirred under mechanical stirring at 40 °C for 8 h. The final product, MgCF@SiO_2/APTES was obtained as a residue and subjected to washing five times with deionized water, acetone, and ethanol.

2.6. Decoration of the third layer-surface of MgCF@SiO_2/APTES with Gallic acid

The sol–gel method was employed to modify MgCF@SiO_2/APTES nanoparticles. The process began by dispersing 0.903 g of nanoparticles in 50 ml of deionized water and was sonicated for 30 min using a sonication bath. After sonication, Gallic acid was gradually added to the mixture at a ratio of 0.5 g GA/20 ml deionized water. The reaction mixture was then subjected to mechanical stirring at 180 rpm and heated to a temperature of 45 °C. The stirring and heating were maintained for 6 h to allow for the desired modifications to occur. Subsequently, the resulting black precipitate was collected using a permanent magnet, and washed with ethanol and deionized water. Finally, the modified nanoparticles oven-dried at 75 °C overnight and stored for further use. The schematic representation of functionalization is shown in Fig. 2.

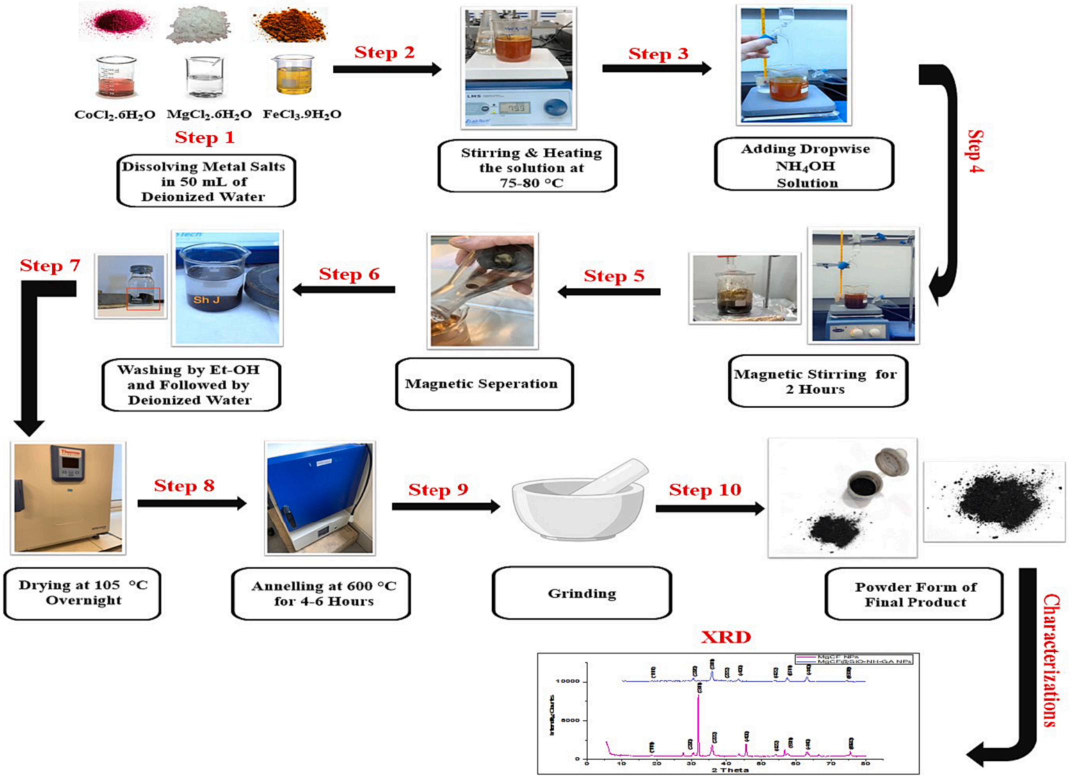

Fig. 1. Schematic representation of the procedure for synthesis magnesium-doped cobalt ferrite NPs.

2.7. Characterization

Various methods were employed to examine and confirm the particle size, distribution, and other relevant parameters of interest in analyzing the as-prepared MgCF@SiO_2-APTES-Gallic acid nano-sorbent. The crystalline structure of the as-prepared nano-sorbent was achieved using X-ray diffraction Philips PW1730 at room temperature. The magnetic characteristics of the nanocomposite were assessed under the influence of an applied magnetic field using an MDKB vibrating sample magnetometer (VSM) at room temperature. Furthermore, the composition of the as-prepared nanocomposite was evaluated by recording infrared spectra over the range of 4000–400 cm^{-1} using a Fourier transform infrared (FTIR) spectrophotometer (Thermo avatar). Transmission electron microscopy was utilized to characterize the particle size and morphology; the procedure was performed using a Philips CM120. Brunauer–Emmett–Teller (BET) model and N_2 adsorption method were used to determine the specific surface area, pore volume, and pore diameter. These parameters were calculated using the analyser BELSORP mini2. Additionally, thermogravimetric analysis (TGA) was conducted to examine the adsorbed mass of the coating and functionalization on the surface of MgCF NPs using a TA instrument, with heating from 25 °C to 1000 °C (at a rate of 10 degrees per minute) in an argon atmosphere.

2.8. Adsorption experiments

The adsorption experiments were conducted by introducing 1 g of the nano-adsorbent into a 250 ml conical flask containing 50 ml of dye solution. The initial pH of the dye solution was adjusted by adding either 0.1 M NaOH or 0.1 M HCl. Subsequently, the solution was agitated at room temperature in an incubator shaker at a speed of 200 rpm until equilibrium was achieved. Following the adsorption process, the samples were collected, and the suspensions were easily decanted using an external magnet. Finally, the removal of dye was assessed.

$$q_e = \frac{(C_o - C_e)V}{W} \tag{1}$$

Where, q_e is Amount of dye adsorbed (mg/g), C_o is Initial dye concentration ($mg.l^{-1}$), C_e is Equilibrium dye concentration ($mg.l^{-1}$), W is Mass of nano-adsorbent (mg), and V is Solution volume (ml).

The removal percentage was determined using the equation below:

$$R\% = \frac{C_o - C_e}{C_o} \times 100 \tag{2}$$

Where, C_o and C_e = are Initial and final dye concentrations ($mg.l^{-1}$), respectively and R% is removal percentage.

2.9. Regeneration investigation

To investigate the regeneration process, we employed a fixed quantity of dyes-loaded MgCF@SiO-NH-GA nano-adsorbent in a conical flask. The flask was then filled with 50 ml of a desorbing solution and placed on a thermostatic shaker at 180 rpm for 30 min. The desorption study was carried out utilizing a mixture of 0.5 g of dyes (MB/RhB)-loaded modified MgCF@SiO-NH-GA and 50 ml of deionized water with controlled pH 11. Subsequently, the mixture was agitated at room temperature overnight using mechanical shaker (VWR incubating orbital shaker). Following this, the solution was filtered, and the nano-sorbent was thoroughly rinsed with deionized water multiple times until it achieved a neutral state. Next, the nano-sorbent was subjected to oven-drying at 105 °C and then followed by adaorption process again.

The percentage regeneration efficiency of the nano-sorbent was calculated using the following formula:

$$\text{Regeneration efficiency} = \frac{\text{Amount of dyes adsorbed in }(\text{n}+1)\text{th cycle}}{\text{Amount of dyes adorben in nth cycle}} \times 100 \tag{3}$$

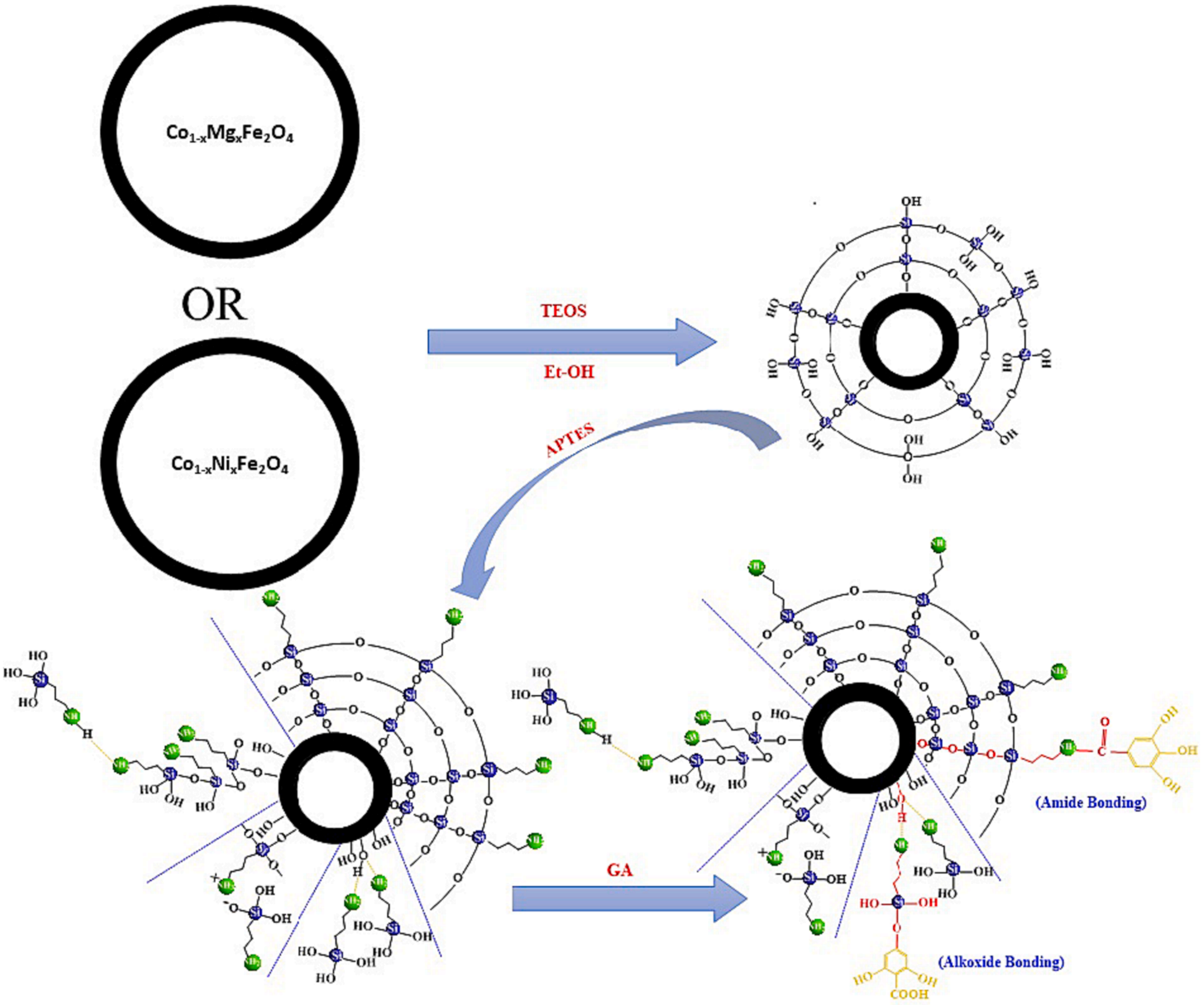

Fig. 2. Schematic representation of the coating of magnesium-doped cobalt ferrite NPs with a silica shell and their subsequent functionalization with Gallic acid.

2.10. *In vitro cytotoxicity assay*

The cytocompatibility of nanoparticles (NPs) on 3 T3 fibroblast cells was assessed using the MTT assay. 3 T3 fibroblast cells were seeded in 96-well plates at a density of 6000 cells per well in 100 μL of DMEM/F12 media supplemented with 10 % FBS. After 24 h of cell attachment, the media was removed, and 0.1 ml of fresh medium containing various concentrations of NPs was added to each well. The cells were then incubated with the NPs for 24 and 48 ho. After the incubation period, the medium was removed, and the wells were washed with PBS buffer at pH 7.4. A solution of MTT (0.5 mg/mL in PBS) was added to each well, and the cells were incubated for 3 h at 37 °C and 5 % CO_2. The formazan crystals formed by viable cells were dissolved by replacing the MTT solution with 0.1 ml of dimethyl sulfoxide (DMSO). The absorbance at 570 nm was measured using a microplate reader (Synergy H1MFD, BioTek Instruments, USA). The absorbance values were normalized to the control (non-treated cells) to calculate the percentage of cell toxicity and cell viability. To calculate the percentage of cell toxicity and cell viability, the following equations were used:

$$\text{Viability\%} = \left(\frac{meanODofsample}{meanODofcontrol}\right) \times 100 \tag{4}$$

$$\text{Toxicity\%} = 100 - \text{Viability\%} \tag{5}$$

3. Results and discussions

3.1. *Structure morphology, and characteristics analysis*

3.1.1. *Transmission electron microscopy (TEM) analysis*

In Fig. 3, TEM images and size distribution analysis of $MgCoFe_2O_4$ NPs and the $MgFe_2O_4$ core–shell structure with Gallic acid decoration (@SiO_2-NH_2) are presented. In Fig. 3a, unmodified MgCF NPs exhibit a spherical morphology, which is evident due to the strong magnetic affinity between the particles. This magnetic attraction results from both van der Waals forces and magnetic dipole–dipole interactions, leading to the aggregation of individual particles to some extent. The mean particle size distribution of 7.9 nm, as shown in Fig. 3b. Fig. 3c,e provides TEM images of MgCF@SiO-NH-GA. These images confirm the core–shell structure of MgCF@SiO–NH-COOH, where the particle sizes have reached to 8.1 nm, and in some instances, the particles are much smaller in size, around 4.53 nm, resembling nano-dots. This size reduction can be attributed to the coating agent, which effectively prevents particle aggregation. Furthermore, it may be due to the blocking of magnetic interactions when the nanoparticles become charged, thereby

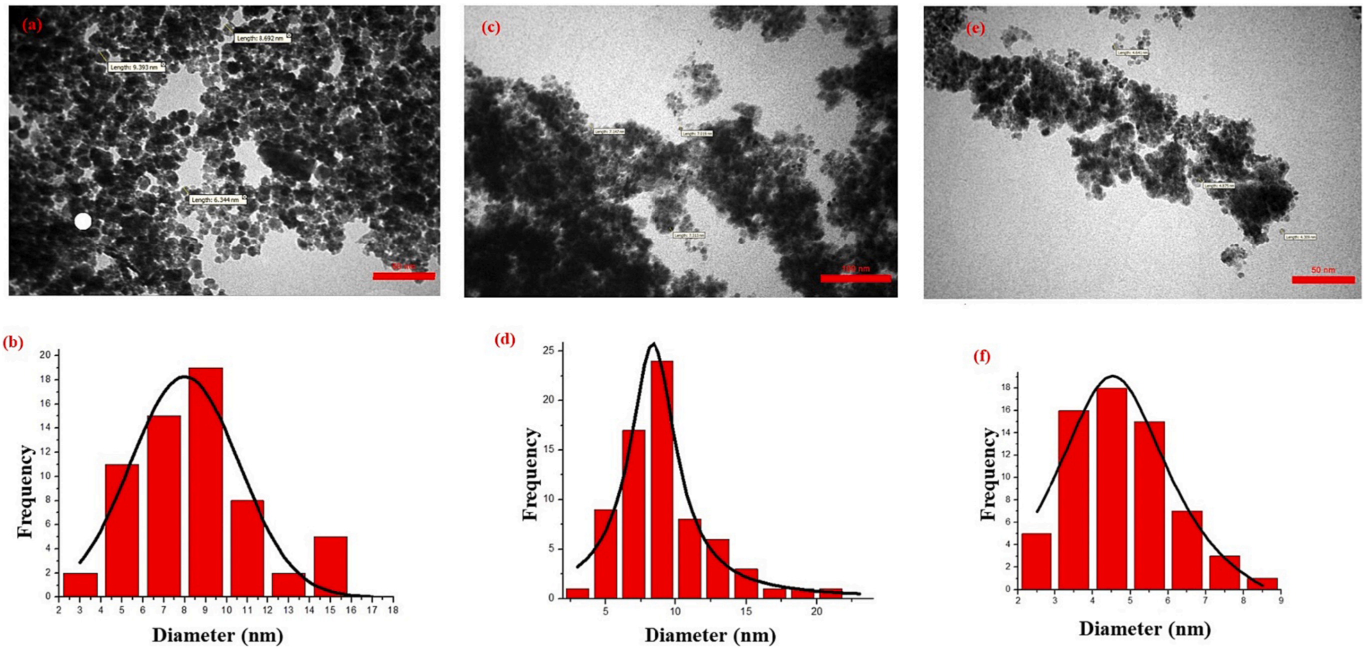

Fig. 3. TEM images of a) MgC NPs and c, e) MgCF@SiO-NH-GA and histogram of the particle size distribution of b) MgC NPs and d, f) MgCF@SiO-NH-GA.

minimizing nanoparticle dimensions. The histogram of the particle size distribution, obtained from measuring 100 units, is shown in Fig. 3b for the unmodified nano-adsorbent and in Fig. 3d,f after modifications. It reveals particle sizes ranging from 4 to 15 nm, with a higher incidence between 4 and 7 nm.

3.1.2. Field emission scanning electron microscopy (FE-SEM)

The FE-SEM analysis of the as-synthesized MgCF NPs (Fig. 4a) revealed a highly globular and spherical morphology. This can be attributed to the solid magnetic affinity between the MgCF nanoparticles, resulting from the interaction forces, including Van der Waals attraction and magnetic dipole–dipole interactions. These forces lead to the aggregation of individual particles to a certain degree. The size and shape of nanoparticles are controlled by the quantities of MgCF and TEOS. The amount of MgCF impacts the dispensability of MgCF@SiO_2 and the number of MgCF cores coated by silica. Conversely, the formation of mesoporous silica involves the hydrolysis and condensation reactions of alkoxy-silane in a mixture of ethanol, H_2O, and NH_4OH, as described by the following equations:

$$Si(OC_2H_5)_4 + H_2O \ \text{->}\ Si(OH)_4 + 4\ C_2H_5O \quad (6)$$

$$Si(OH)_4 \ \text{->}\ SiO_2 + 2H_2O \quad (7)$$

Fig. 4b-d illustrates the morphological changes in the synthesized nanoparticles before and after adsorbing MB and RhB. The core/shell nanoparticles display a diverse morphology with a spherical shape, exhibiting a rugged surface and high porosity that these attributes enhance their adsorption capabilities. Moreover, the nanocomposites exhibit generations of dendrimer on the surface of the magnetite nanocomposites. This result is a strong evidence of the successful surface modification of the magnetite nanocomposites.

3.1.3. Vibrating sample magnetometer (VSM)

The magnetic properties of the MgCF, MgCF@SiO-NH_2, and MgCF@SiO-NH-GA NPs samples were evaluated utilizing the vibrating sample magnetometer (VSM) patterns, as shown in (Fig. 5) and (Table 1), at room temperature. The primary focus in practical applications is ensuring that the core/shell material has adequate magnetic and superparamagnetic properties.

The saturation magnetization intensity of MgCF, MgCF@SiO-NH_2, and MgCF@SiO-NH-GA NPs was found to be 24.8217, 19.1681, and 15.2971 emu/g, respectively. The observed variation in saturation magnetization among these nanocomposites can be attributed to the differences in the thickness of the coatings during their production. The result indicates that the saturation magnetization of MgCF@SiO-NH-GA is lower than that of MgCF@SiO-NH_2, and the magnetization of MgCF@SiO-NH_2 is lower than that of MgCF NPs. These reductions in magnetism characteristics confirm amine and carboxyl functional sites on the MgCF@SiO-NH_2 and MgCF@SiO-NH-GA nanocomposites. However, despite the drop in saturation magnetization, MgCF@SiO-NH-GA still exhibits a high level of magnetism, enabling its effective separation in recycling studies with an external magnetic field. The obtained results confirm the superparamagnetic behavior of the magnetite core. Surface modification of MgCF with TEOS, APTES, and Gallic acid results in the formation of a SiO_2 shell and generations of dendrimers on the magnetite nanoparticles' surface, leading to a reduction in saturation magnetization. This reduction can be attributed to the weight contribution from the non-magnetic properties of the SiO_2 and dendrimers crust, which is added to the surface of the magnetite nanoparticles (Rashdan and Hazeem, 2020).

3.1.4. Nitrogen adsorption-desorption studies

The surface area, pore volume, and pore radius were determined through nitrogen adsorption–desorption experiments conducted on both the obtained MgCF NPs and the modified MgCF@SiO-NH-GA nanocomposite (Fig. 6). In addition, BET and BJH (Barrett-Joyner-Halenda) techniques were employed to analyze the surface area and pore size distribution, considering both desorption and adsorption branches of the N_2 isotherms. For the as-prepared MgCF NPs, the calculated values for surface area, total pore volume, and pore radius are 14.625 m^2/g, 0.075134 cm^3/g, and 20.549 nm, respectively.

The results for BET and Horvath-Kawazoe (HK) analysis of the modified MgCF@SiO-NH-GA (shown in the figure inset) reveal a distinct type IV isotherm pattern with a corresponding H_2-type hysteresis loop. This is characterized by a shift in nitrogen adsorbed volume occurring at a relative pressure (P/P0) of 0.990, confirming the formation of mesopores with diameters ranging from 2 to 50 nm. The surface area and pore volume of the mesoporous MgCF@SiO-NH-GA nanocomposite were determined to be 31.655 m^2/g and 0.13 cm^3/g, respectively. This

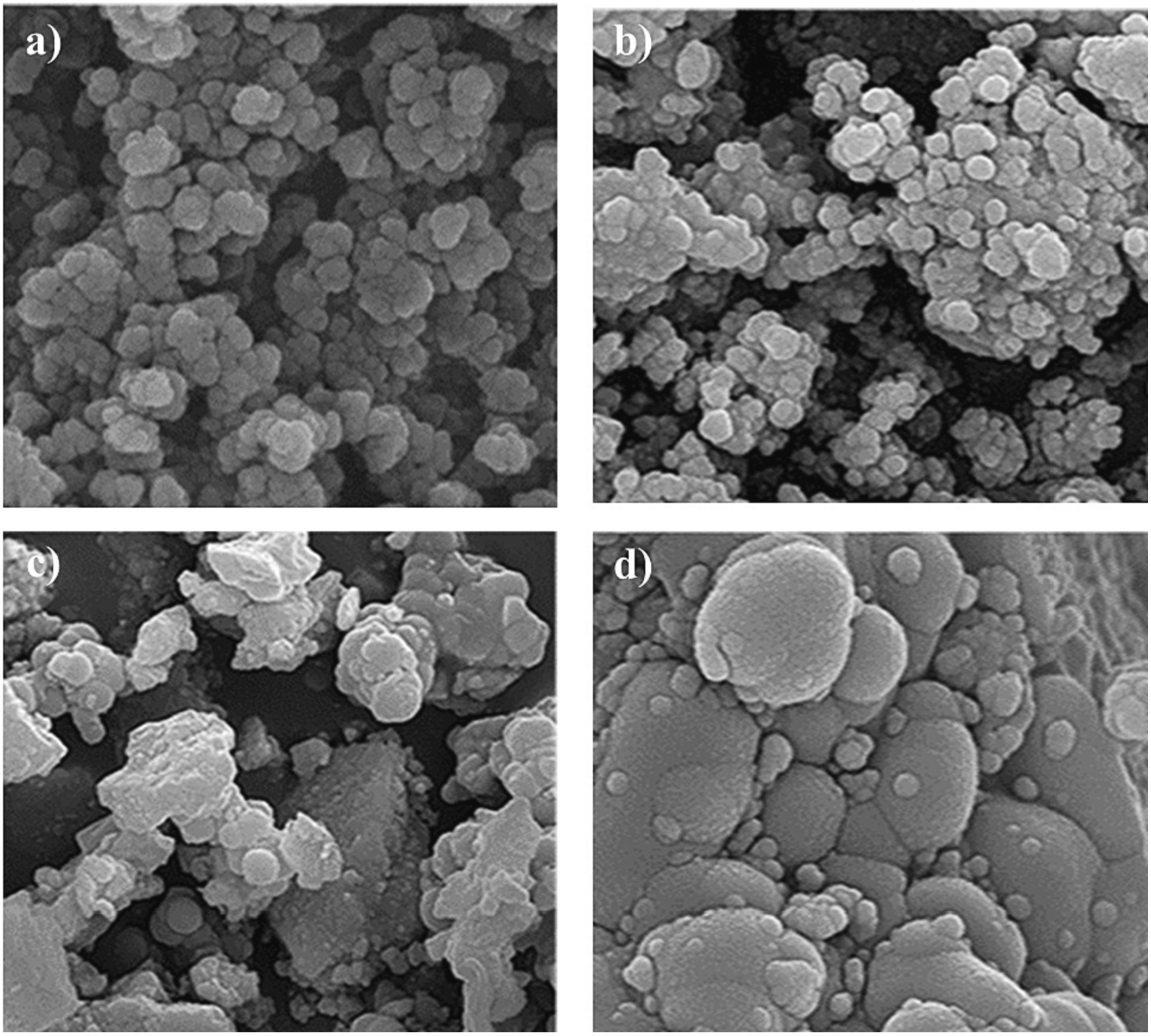

Fig. 4. FE-SEM images of a) MgCF NPs, b) MgCF@SiO-NH-GA NPs, c, d) MgCF@SiO-NH-GA NPs after adsorption MB and RhB, respectively.

indicates a relatively high surface area, which could significantly enhance the adsorption capacity for MB and RhB from aqueous solutions. Notably, BET analysis also revealed the presence of mesopores with an average diameter of 17.044 nm in the produced nanoadsorbent. Therefore, the combination of a high surface area and a mesoporous structure in the as-prepared MgCF@SiO-NH-GA NPs positions it as a promising candidate for a heterogeneous catalyst in wastewater treatment procedures.

3.2. *Adsorption study*

Firstly, we compared the adsorption capability of nan-adsorbent after various modifications. Fig. 7 a, b show the adsorption capacity (qe) and the removal percentages of MgCF, MgCF@SiO, MgCF@SiO-NH, and MgCF@SiO-NH-GA for the removing of MB and RhB dyes. The results clearly confirm the higher performance of MgCF@SiO-NH-GA for the adsorption of both dyes.

In the next step, an adsorption study was carried out to examine the adsorption capacity for MB and RhB on as-synthesized MgCF NPs and MgCF@SiO.NH-GA nanocomposite as shown in (Fig. 8a-f).

The MgCF@SiO-NH-GA nanocomposite displays a rapid adsorption rate and higher adsorption capacity for MB and RhB organic dyes. Moreover, the as-synthesized MgCF nanoparticles have a positively charged surface. As SiO_2/NH_2-GA is attached onto the surface of the $CoFe_2O_4$ nanoparticle, multiple negative COO and OH groups on GA alter the surface of the MgCF@SiO-NH-GA nanocomposites to charge negatively. Correspondingly, as-synthesized NPs exhibit a deficient adsorption capacity in comparison with the functionalized and decorated nanocomposite for dye removal. The nanocomposites also have the highest specific surface area since the particle sizes are inversely proportional to their specific surface areas. MgCF@SiO-NH-GA has the highest adsorption capacity (53.3 mg.g^{-1}) because of its smallest particle size and largest specific surface area. Meanwhile, the maximum adsorption capacity for dyes of MgCF@SiO-NH-GA nanocomposite is higher than that of as-synthesized MgCF NPs. Additionally, the removal rates for MB and RhB onto the MgCF@SiO-NH-GA are 96.3 % and 92.0 %, respectively (Fig. 8a).

3.3. *Optimization of pH*

Several factors, including pH, point of zero charge (pHpzc), contact time, initial dye concentrations, adsorbent mass, and temperature, play a significant role in the removal process. Optimizing the pH level and determining the pH$_{pzc}$ (pH at the point of zero charge) of the nano-

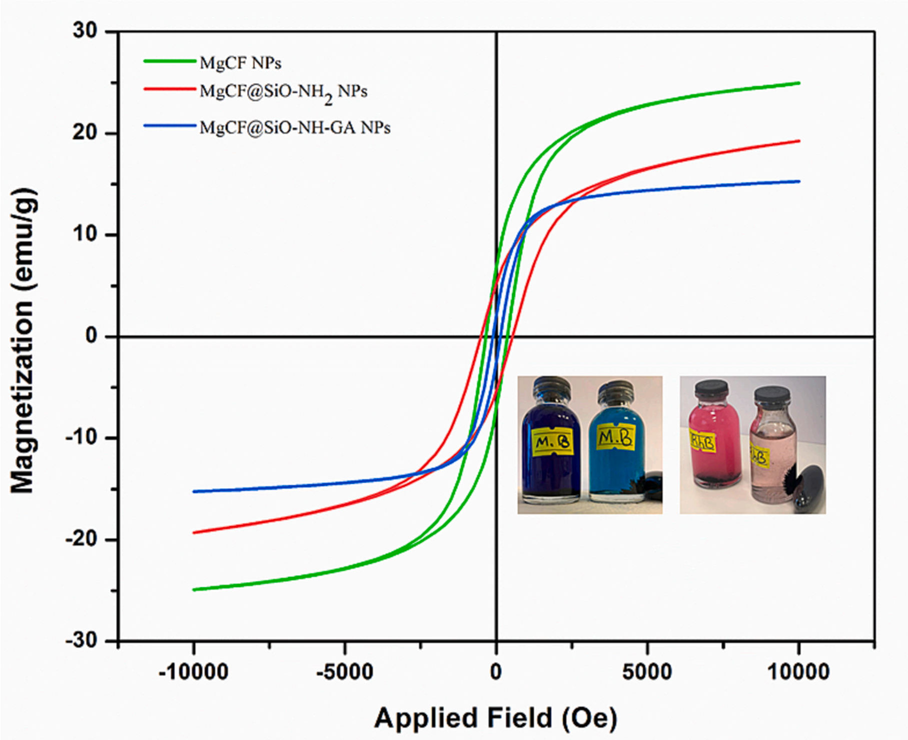

Fig. 5. VSM Curves of MgCF, MgCF@SiO-NH$_2$, and MgCF@SiO-NH-GA NPs.

Table 1
Magnetic parameters of MgCF, MgCF@SiO-NH$_2$, MgCF@SiO-NH-GA NPs.

Samples	Saturation Magnetization (Ms)	Remanence Magnetization (Mr)	Coercivity (Hc)
MgCF	24.8217 emu/g	5.9377 emu/g	344.8886 Oe
MgCF@SiO-NH$_2$	19.1681 emu/g	4.7976 emu/g	516.9498 Oe
MgCF@SiO-NH-GA	15.2971 emu/g	1.4301 emu/g	117.1986 Oe

adsorbent are critical for enhancing the removal procedure. The pH of the solution is a critical factor in the adsorption process, exerting a strong influence on the removal mechanism, including the surface sites and charge type of the adsorbate (nanocomposite). It can induce either an increase or reduction in the efficiency of MB and RhB removal. In bench-top experiments, 100 mg of MgCF@SiO-NH-GA was stirred with 100 ml of a 50 mg/L dye solution under varying pH conditions (pH 2–12). As shown in Fig. 8b, the removal percentage of MB and RhB increased as the pH level rose. At a neutral pH, the removal percentages for MB and RhB reached 99 % and 98 %, respectively. Both MB and RhB dyes belong to the category of cationic dyes, capable of ionizing into chloride ions (Cl^{-}) and dye cations (such as positively charged MB + and RhB + ions). Consequently, at pH levels higher than 7, both dyes primarily exist in their cationic forms as MB + and RhB + ions. Conversely, when the pH falls below 7, the nanocomposite becomes positively charged, leading to enhanced repulsive forces between dye molecules and these positively active sites on the surface of the MgCF@SiO-NH-GA, resulting in reduced dye removal efficiency. Additionally, the

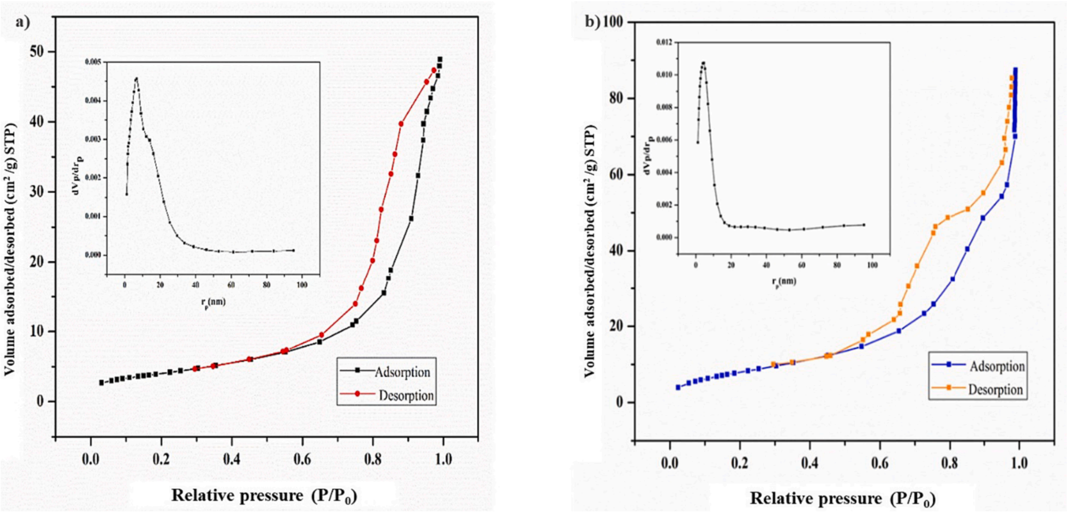

Fig. 6. Nitrogen adsorption/desorption isotherm and pore size distributions (inset) a) MgCF and b) MgCF@SiO-NH-GA particles.

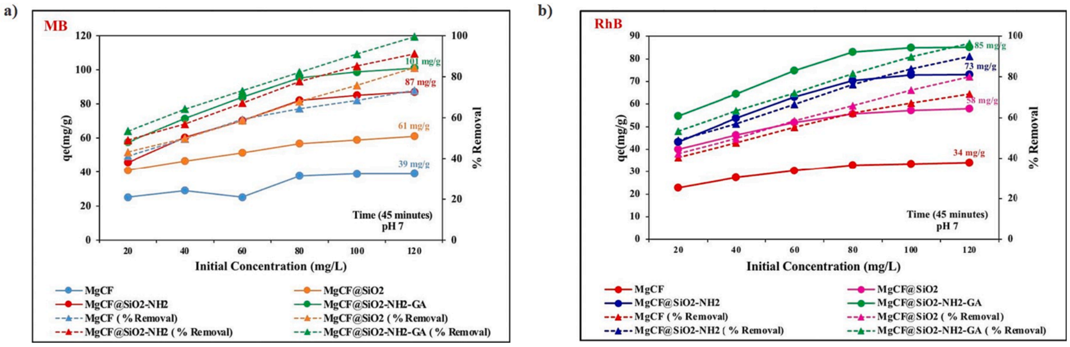

Fig. 7. The adsorption capacity and the removal percentages of MgCF, MgCF@SiO, MgCF@SiO NH, and MgCF@SiO NH-GA for the removing of MB and RhB dyes.

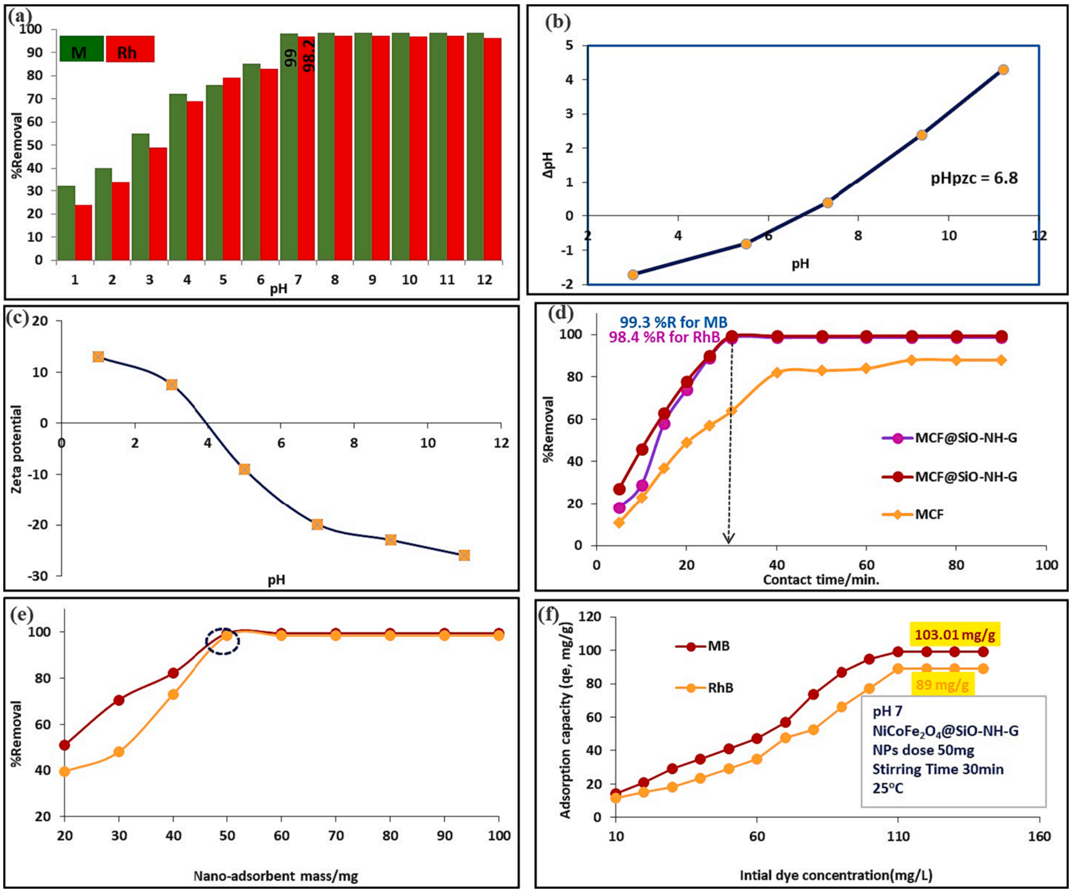

Fig. 8. (a) Effect of pH on dyes (MB and RhB) adsorption onto MgCoFe$_2$O$_4$@SiO-NH-GA. (b) Determination of pHzpc of the nano-adsorbent (MgCoFe$_2$O$_4$@SiO-NH-GA). (c) Zeta potential of MgCoFe2O4@SiO-NH-GA NPs as a function of solution pH at room temperature. (d) Effect of contact time. (e) Effect of nano-adsorbent mass onto dyes adsorption. (f) Effect of initial dyes concentration onto adsorption process at pH 7.

lower adsorption capacity and removal percentage observed at pH levels below 7 could be attributed to the competition between H^+ ions and dye + ions at surface sites. In contrast, when the pH is equal to or greater than 7, the surface of the MgCF@SiO-NH-GA shifts towards negative charges, as confirmed by Zeta Potential measurements. This alteration enhances the adsorption of cationic MB and RhB dyes.

At an acidic medium, the adsorption of RhB on composite is greater than in the basic solution. It is justified by the fact that when the dye solution changes its pH, numerous ionic species are formed in the solution. At lower pH, the cationic and monomeric forms of RhB exist and it interact with the negatively charged adsorbent. On the other hand, at higher pH, RhB exits in the zwitterionic form in water and causes an accumulation of dye molecules that leads to dimmer formation (Rani et al., 2023).

Consequently, the dyes' sorption by MgCF@SiO-NH-GA NPs was most effective at pH values greater than 7, with only a slight difference in removal percentage between pH 7 and pH > 7. Therefore, pH 7 was chosen as the most suitable condition for subsequent studies. The surface of the adsorbent becomes actively involved in reactions that include cation attraction and exchange, facilitated by the strong electrostatic interactions between the cationic dyes and the negatively charged active sites of the nano-adsorbent. This reduction in the hindrance to the diffusion of dye molecules (MB and RhB) results in a significant increase in adsorption capacity.

3.4. Zeta potential (ZP) measurements

Fig. 8c illustrates the compatibility of the MgCF@SiO-NH-GA nano-adsorbent for effective cationic toxin adsorption under neutral conditions. In contrast, the measured point of zero charge at pH 7 was −19.9 mV. Consequently, the MgCF@SiO-NH-GA nano-adsorbent could provide an effective and straightforward removal method for cationic dyes such as MB and RhB.

3.5. Effect of contact time

The effect of stirring time on the adsorption of MB and RhB was also examined, as the stirring time plays a significant role in the binding of MB/RhB dye molecules to the functionalized nanocomposite and, accordingly, their dye adsorption capacity. In contrast, bench-top experiments involved agitating 50 mg of MgCF@SiO-NH-GA with a 50 mg/L dyes (MB/RhB) solution/50 ml for durations ranging from 5 to 90 min (pH neutral condition). Meanwhile, the findings revealed that the highest percent removal was achieved within 30 min, as can be seen from (Fig. 8d) that the nano-adsorbent (MgCF@SiO-NH-GA) effectively attached 99 % and 98.2 % for MB and RhB dyes, respectively. These results suggest that the removal of MB/RhB occurs rapidly at the initial stages and then slows down before reaching the saturation stage at 60. Furthermore, this effect confirms that the adsorption of MB/RhB is a rapid process and time-dependent. Nevertheless, the lower efficiency observed at stirring times less than 30 min may be attributed to insufficient contact time between the MB/RhB molecules and the nano-adsorbent.

3.6. Effect of nano-adsorbent (MgCF@SiO-NH-GA) mass

The concentration of MgCF@SiO-NH-GA nano-adsorbent has the potential to influence the removal percentage of MB and RhB dyes. We adjusted the quantity of the nano-adsorbent from 20 to 100 mg under specific conditions: pH 7, room temperature, and a dye concentration of 40 mg/L for both cationic dyes. As illustrated in (Fig. 8e), an increased dosage of MgCF@SiO-NH-GA led to a noticeable improvement in the removal percentages. Conversely, at lower MgCF@SiO-NH-GA dose, the dye adsorption was negligible due to a shortage of cavities and active sites at the surface. In this particular instance, it was observed that 50 mg of MgCF@SiO-NH-GA exhibited the highest dye removal efficiency (99 and 98 % for both MB and RhB). As a result, there is no need to further increase the quantity of the nano-adsorbent in future experiments, as the percentage of dye removal remained relatively constant.

3.7. Effect of dye (MB and RhB) concentrations

The initial concentrations of dyes (MB and RhB) are pivotal in exerting a controlling influence to mitigate resistance between the dye solution and the solid nano-adsorbent. Therefore, bench-top experiments were conducted by varying the initial concentrations within the range of 10 to 100 mg/L to assess the maximum adsorption capacity (mg/g) of the proposed nano-adsorbent. In contrast, keeping other parameters constant. The results presented in Fig. 8f reveal that the adsorption of MB and RhB increases as the dye concentration rises, reaching an equilibrium stage with a maximum adsorption capacity of 103 mg/g for MB and 89 mg/g for RhB, respectively. At higher dye concentrations, a slight increase in adsorption is observed due to the competition among a significant quantity of MB and RhB molecules for the surface-active sites on the nano-adsorbent.

3.8. Isotherm-models study

In this study, we examined the surface-active sites of the as-prepared nano-adsorbent (MgCF@SiO-NH-GA) and their interaction with MB and RhB in aqueous phases during the adsorption process. We employed two commonly used isotherm models, namely Langmuir and Freundlich. The Freundlich isotherm model helped us understand the adsorption behavior of heterogeneous systems, focusing on the relationship between q_e and C_e. This provided insights into the heterogeneous nature of the MgCF@SiO-NH-GA surface. On the other hand, the Langmuir model explains the adsorption behavior of homogeneous systems, specifically monolayer chemical interaction. Our study investigated the interaction between MB, RhB dyes, and the nano-adsorbent under optimal sorption conditions, with dye concentrations ranging from 10 to 100 mg/L. We utilized the linear Langmuir and Freundlich models to analyze the equilibrium phase of the MB and RhB-NPs interaction.

$$\ln qe = \ln K_F + \frac{1}{n}\ln C_e \tag{8}$$

$$\frac{C_e}{q_e} = \frac{1}{K_L Q_o} + \left(\frac{1}{Q_o}\right) C_e \tag{9}$$

$$R_L = \frac{1}{1 + K_L C_o} \tag{10}$$

The Freundlich constants K_F and n represent the adsorption ability of the nano-adsorbent (MgCF@SiO-NH-GA) and the sorption efficiency, respectively. On the other hand, Q_o and K_L stand for the maximum abilities of the nano-adsorbent (mg.g^{-1}) and the sorption equilibrium constant (L.mg^{-1}). These parameters were determined in this study by analyzing the slope and intercept of the linear figures obtained, and the results are recorded in Table 2.

Based on the correlation coefficients (R^2) shown in Fig. 9a, b, the Langmuir isotherm model provided an excellent fit to the experimental data (0.9912 and 0.9946 for RhB and MB, respectively), while the Freundlich isotherm model had a relatively lower R^2 value (Fig. 9c,d).

The theoretical maximum adsorption capacities (Q_o) were 105 and 118.7 mg.g^{-1}. These values closely matched the experimental values of 103 and 89 mg.g^{-1} for both MB and RhB, respectively. Therefore, it can be inferred using 0.5 g of the used nano-adsorbent can adsorb approximately 0.125 g and 0.141 g of MB and RhB from natural wastewater, respectively. The obtained data also indicated that the KL values were less than 1, suggesting the reversibility of MB and RhB adsorption. Additionally, the 1/n values were lower than 1, demonstrating that the adsorption nature of MB and RhB is chemisorption and favorable. The recorded R_L value between 0 and 1 further supports the favorability of the adsorption process.

3.9. Kinetic studies of dyes (MB/RhB) removal

The specific adsorption process plays a crucial role in practical applications. It can be studied using dynamic adsorption models. The kinetic study of dyes (MB/RhB) adsorption was conducted to characterize the adsorption performance in terms of stability over time, the type of interaction and binding mechanism with the nano-adsorbent (MgCF@SiO-NH-GA), and the sorption rate, which involve adding 0.1 g of freshly prepared nano-adsorbents into a 15 ml dyes solution (20 mg. l^{-1}) at pH of 7. The residual content of dyes (MB/RhB) was measured using a UV–Vis spectrophotometer. The resulting adsorption capacities are then analyzed using pseudo-first and pseudo-second kinetic models. This comparison of the two kinetic models allows for a deeper understanding of the specific adsorption process.

The kinetic equations (pseudo-first and pseudo-second) are given as follows:

$$\log(q_e - q_t) = \log q - \left(\frac{k1}{2.303}\right) t \tag{11}$$

$$\frac{t}{q_t} = \frac{1}{\left(k_2 q_e^2\right)} + \frac{t}{q_e} \tag{12}$$

Table 2
Langmuir and Freundlich adsorption isotherm parameters.

	MB					Rh-B				
Langmuir isotherm model	**Q_o (mg.g^{-1})**	**q_m (mg.g^{-1})**	**R^2**	**K_L (L.mg^{-1})**	**R_L**	**Q_o (mg.g^{-1})**	**q_m (mg.g^{-1})**	**R^2**	**K_L (L.mg^{-1})**	**R_L**
	118.7	103.01	0.997	0.699	<1	105	89	0.992	0.297	<1
Freundlich isotherm model	**K_F**	**1/n**	**R^2**	**n**		**K_F**	**1/n**	**R^2**	**n**	
	58.72	0.29	0.918	3.44		28.91	0.47	0.968	2.12	

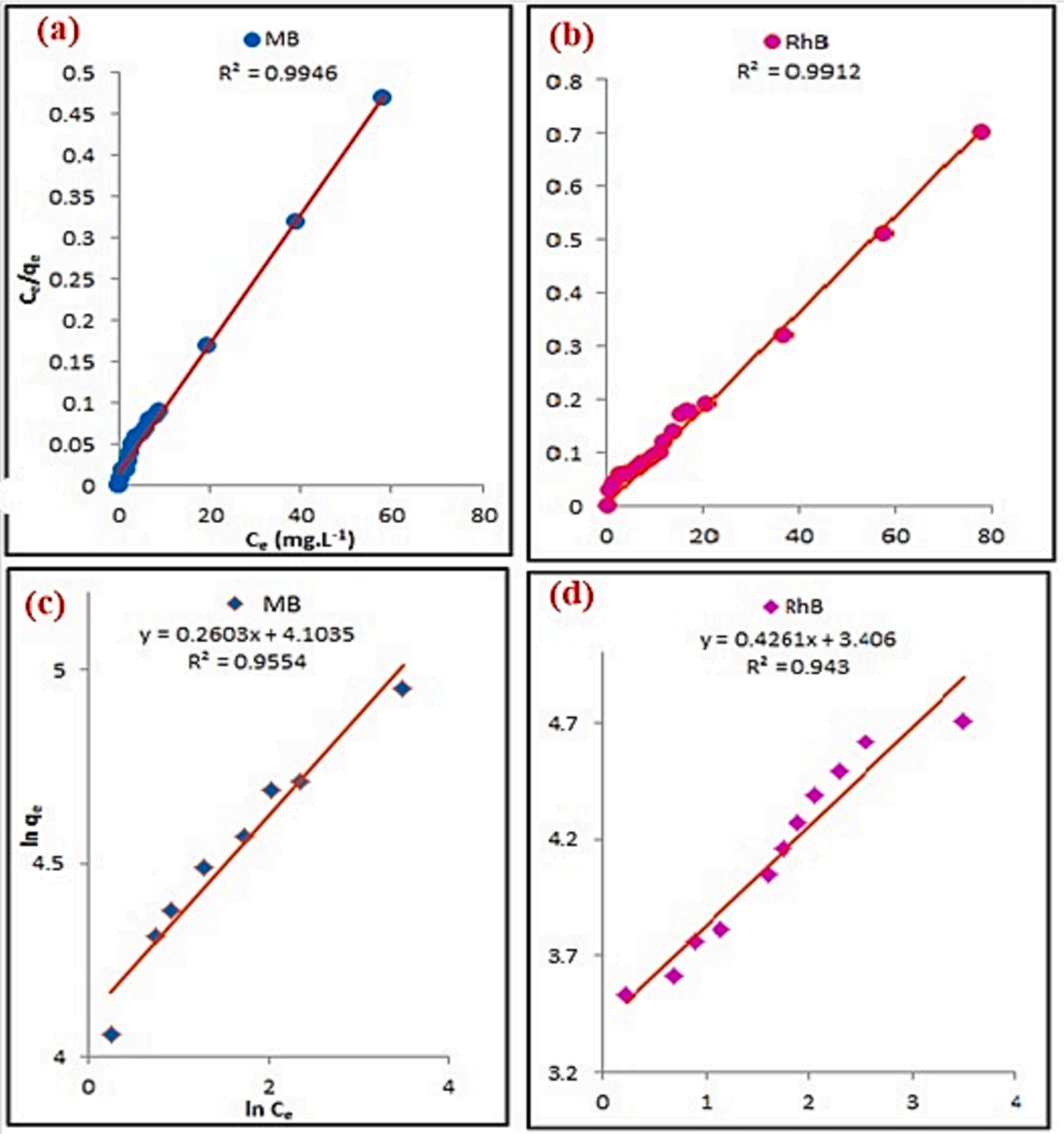

Fig. 9. Adsorption isotherm model a, b) Langmuir and c, d) Freundlich isotherm model of adsorption MB and RhB by MgCF@SiO-NH-GA.

Where q_e (mg·g^{-1}) is the adsorption capacity at the equilibrium state, q_t (mg·g^{-1}) is adsorption capacity at time t, K_1 and K_2 are rate constants of pseudo-first and second kinetics, respectively. The obtained profiles demonstrate a two-stage adsorption behavior, the data obtained (Fig. 10) indicated that during the first 30 min, the sorption was rapid due to the availability of active surface sites of the nano-adsorbent then

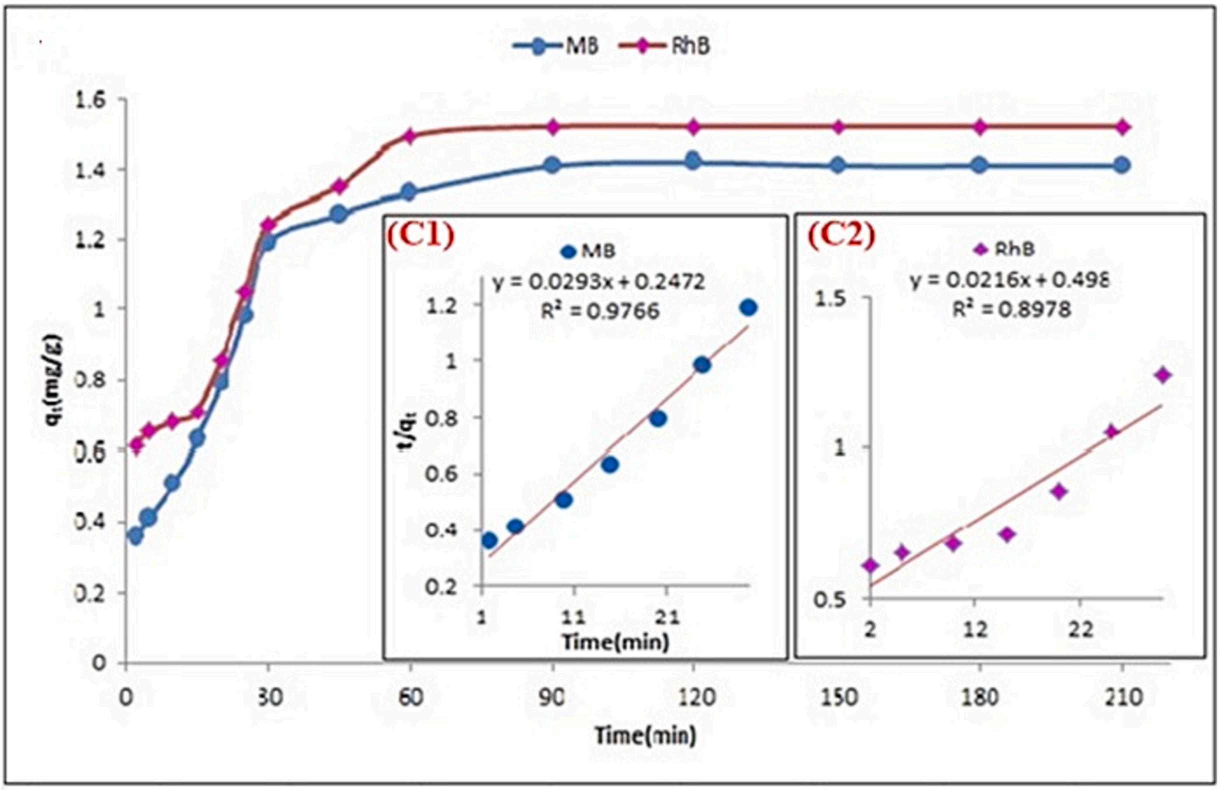

Fig. 10. Adsorption kinetics adsorption-capacity versus time. (C1 and C2) Inset: fitting of pseudo-second order kinetic model).

followed by a slower adsorption process until reaching saturation stage, as previously discussed in the study of the stirring time parameter. The pseudo-second-order model is employed to evaluate the nature of adsorbent-adsorbate interaction and identify a rate-limiting step.

Furthermore, to better understand the adsorption mechanism based on kinetic models, this behavior suggests that the adsorption process occurs not only on the surface of the nano-adsorbent (MgCF@SiO-NH-GA), confirming previous findings. Notably, a significant amount of dyes (MB/RhB) is adsorbed in the first stage within a few minutes. This can be attributed to the abundance of unoccupied mesopores and available adsorption sites, particularly the covalently bonded amino and carboxylic groups that exhibit strong interactions with dye ions, facilitating the initial rapid adsorption process. In contrast, when the mesopores of the nano-adsorbents are fully modified, any remaining of dye ions will start to penetrate deeper into other existing microspores. This phenomenon introduces a more vigorous resistance, resulting in a slower adsorption rate in the second stage. Furthermore, once all the grafted of carboxylic and amino groups are saturated, the adsorption capacity reaches a constant level, representing the final state of the kinetic curve. The findings demonstrate that a significant portion of dye ions can be eliminated within the initial first 30 min of contact. Next, the concentration of the supernatant stabilizes, indicating that the uptake of dyes (MB/RhB) remains nearly unchanged as the contact time increases. This suggests that all available adsorption sites have been nearly saturated. Additionally, (Fig. 10 and Table 3) showed that the adsorption of dyes (MB/RhB) follows pseudo-second order kinetics, as indicated by the high R^2 values. This suggests that the removal/adsorption mechanism of dyes ((MB/RhB)) using MgCF@SiO-NH-GA involves chemical adsorption. This behavior can be attributed to the rapid binding of dye ion with the surface-active sites of MgCF@SiO-NH-GA and the increased diffusion/transfer rate of these dyes. The rate constant for dye molecules (diffusion) also indicates a chemosorption interaction, with the significant value of k_2 confirming a faster sorption rate.

Table 3
Pseudo- first order, Pseudo-second order, intra-particle diffusion and Boyd model parameters based experimental data.

MB			RhB		
		Pseudo-first order model			
$k_1(min^{-1})$	$q_e(mg/g)$	R^2	$k_1(min^{-1})$	$q_e(mg/g)$	R^2
0.00499	113.7	0.9286	0.00583	97.2	0.8665
		Pseudo-second order model			
$K_2(g.mg^{-1}.min^{-1})$	$q_e(mg/g)$	R^2	$k_2(g.mg^{-1}.min^{-1})$	$q_e(mg/g)$	R^2
$2.85 * 10^{-3}$	31.59	0.9766	$8.2 * 10^{-4}$	47.5	0.8978
		Intra-particle diffusion model			
K_{id} (mg/g.min$^{1/2}$)	C_i / (mg/g)	R^2	K_{id} (mg/g.min$^{1/2}$)	C_i / (mg/g)	R^2
0.598	0.574	0.9652	2.193	6.261	0.9128
		Boyd model			
R^2				R^2	
0.9766				0.9804	

3.10. Diffusion mechanism and kinetics

The adsorption process involves various mechanisms, including, intra-particle diffusion, film diffusion, bulk diffusion, and adsorption by active sites on the adsorbent's interior face. Thus, to determine the actual diffusion mechanism during adsorption, the intra-particle diffusion and Boyd models are commonly used. The dominance of intra-particle diffusion as the rate-governing step can be confirmed by plotting q_t against $t^{1/2}$, resulting in a straight line passing through the origin (Equation (11). The slope of this line represents the rate constant of intra-particle diffusion (k_{id}, mg/g.min$^{1/2}$), while the intercept provides information about the boundary layer thickness (C_i, mg/g). Regarding the adsorption of cationic dyes by nano-adsorbent ($MgCoFe_2O_4$@SiO-NH-GA), the plots show two linear regions with different slopes. However, none of the lines passes through the origin ($C_i \geq 2.204$ mg/g) (Table 3), indicating the involvement of at least two significant steps in the adsorption process (Fig. 11a).

The first linear portion corresponds to dye diffusion from the solution to readily accessible binding sites on the external surface of the carboxyl, amine-nanosorbent even the silica-coated. In contrast, the second linear region represents dye diffusion into less accessible internal pores until the equipoise is reached. The narrowest boundary layer is observed for MB, which can easily penetrate the interior face of nano-adsorbent due to its small size and symmetrical structure. On the other hand, more significant dyes exhibit a greater boundary layer thickness, indicating a higher level of boundary layer control, the Boyd model helps identify the slowest step in the adsorption process. It involves plotting B_t against time t (Equation (12), where B_t represents the fraction of dye adsorbed onto nano-adsorbent at a given time, calculated by the ratio q_t/q_e. The Boyd plots for the adsorption of the dyes (MB/RhB) onto nano-sorbent are linear (Fig. 11b), indicating a correlation between Bt and time. However, these plots do not intersect the origin, suggesting that external mass transfer, primarily governed by film diffusion, is the rate-controlling mechanism for the removal of dyes by the sorbent-NPs.

$$q_t = k_{id} t^{\frac{1}{2}} + C_i \tag{13}$$

$$B_t = -0.4977 - \ln(1 - F) \tag{14}$$

3.11. Effect of recycling of MgCF@SiO-NH-GA on the removal process

The recycling and regeneration achievement of nano-adsorbent is also a critical index to investigate the role of the adsorbent. Accordingly, it is essential to evaluate the recycling of MgCF@SiO-NH-GA. Here, the recycling process carried out under the conditions: initial dye concentration of 20 mg/L, nano-adsorbent dosage 0.5 g, initial solution pH 7, temperature 298 K and contact time 0.5 h. Furthermore, in basic media the hydroxide ions easily compete with the negatively active adsorption sites on the surface of MgCF@SiO-NH-GA to adsorb dyes ion. In this work, 0.01 mol/L sodium hydroxide solution was utilized as an elution solution to address the adsorption material. (Fig. 12) indicates the removal efficacy of MB/RhB dyes onto as-synthesized MNPs at the first stage was 98.6 % (MB), 95.3 % (RhB) and after five regenerations still was 82.5 % (MB) and 79.6 (RhB), which elucidates that the MNPs (MgCF@SiO-NH-GA) has excellent recycling and regeneration performance.

Nevertheless, the results displayed that the development of magnetic MgCF@SiO-NH-GA nanocomposite is substantially remarkable. Table 4 shows the compares of the reduction of MB and RhB using MgCF@SiO-NH-GA and catalysts reported in the literature.

3.12. MTT assay

MgCF@SiO–NH-GA prepared in the concentration of 25, 50, 100, 250, and 500 μg/mL was used to investigate the cytoxicity. Deionized water was used as the control. When cells attained 70–80 % confluence, the cells were exposed to nanoparticles after 24 and 48 h. Twenty-eight microliters of MTT dye (Sigma-Aldrich, Merck CT01-5,KGaA, Darmstadf, Germany) (2 μg/mL) was added. As Fig. 13 shown, the cell viability percentage have not been changed at the presence of different concentrations of MgCF@SiO–NH-GA nanoparticles after 24 and 48 h.

4. Conclusion

In this study, magnetic magnesium-doped $CoFe_2O_4$ nanoparticles synthsized using a co-precipitation method and the surface of nanoparticles coated with a silica shell matrix and functionalized with amino groups through the application of 3-Aminopropylethoxysilane. The introduction of Gallic acid for enhanced adsorption capabilities was a strategic highlight. The MgCF-SiO_2-APTES-GA nanocomposite has demonstrated significant potential as an exceptionally efficient magnetic nano-adsorbent, exemplified by its excellent performance in

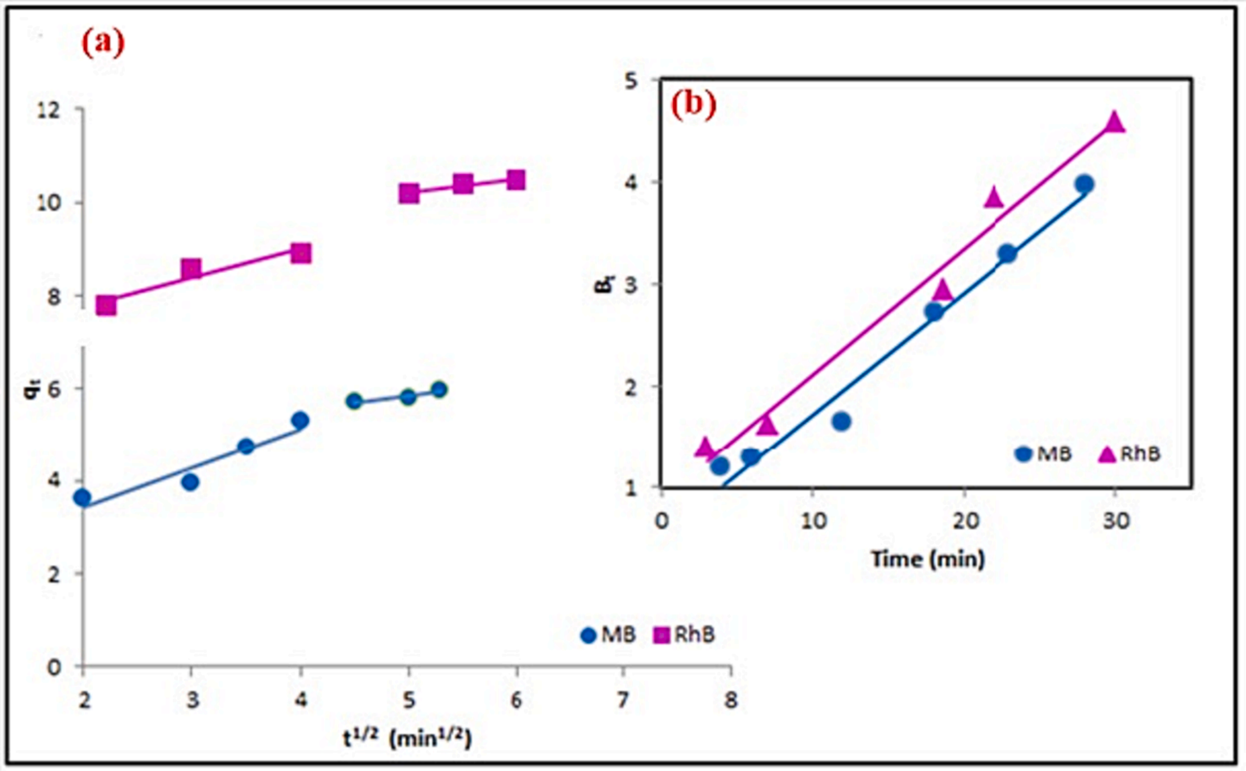

Fig. 11. The effect of contact time on MB and RhB adsorption capacity; a) Intra-particle diffusion model and b) Boynd model.

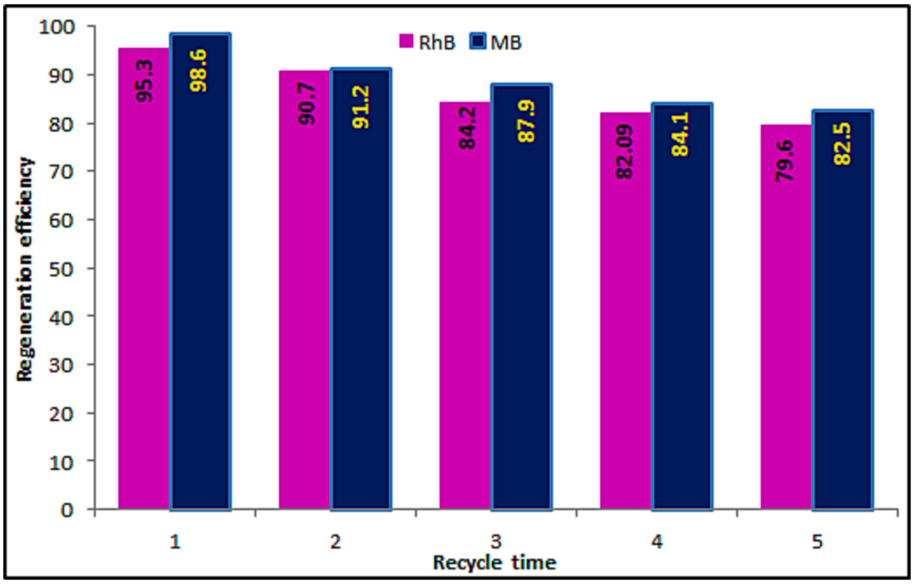

Fig. 12. Effect of regeneration efficiency on the adsorption process.

Table 4
Comparison of the adsorption of MB and RhB in the presence of various catalysts.

Dye	Adsorbent	% Removal	Contact Time	Initial Concentration	Adsorbent Dosage	pH	Temperature	Adsorption Capacity	References
MB	$CoFe_2O_4$	98	7 Minutes	–	0.034 g	7	–	–	(Shojaei et al., 2023)
MB	ZnO-Chitosan Nanocomposites	99.95	160 Minutes	100 mg/L	1 g	8	–	97.93 mg/g	(Zango et al., 2022)
MB	$MnFe_2O_4$/rGO-BC	98.6	15 Minutes	10 mg/L	1 g	7	27 °C	74.626 mg/g	(Tara et al., 2023)
MB	$MnFe_2O_4$	–	270 Minutes	350 mg/L	–	5.5	–	89.29 mg/g	(Thy et al., 2020)
MB	Grown bamboo (Gigantochloa spp.)	80.6	180 Minutes	20 mg/L	0.04 g	7	–	86.6 mg/ g	(Suhaimi et al., 2022)
MB	$CuFe_2O_4$	77	60 Minutes	100 ml of MB aqueous solution (10 ppm)	0.3 g	7	–	–	(Nasrollahi et al., 2019)
MB	$MnFe_2O_4$	96.4	90 Minutes	2 mg/L	0.1 g	6	–	371.7 mg/g	(Jyothi et al., 2019)
MB	Activated carbon from Acacia erioloba seedpods	77.22	2 Hours	10 mg/L	0.01 g	7	30 ± 1 °C	249.67 mg/g	(Daniel et al., 2023)
MB	Graphene oxide incorporated cellulose acetate beads	92	2 Hours	50 mg/L	5 mg	7	25–55 °C	369.85 mg/g	(Eltaweil et al., 2023)
RhB	$Zn_xMn_{1-x}Fe_2O_4$	99	180 Minutes	20 mg/L	1 g	3	–	–	(Jasim et al., 2023)
RhB	Coconut shell activated carbon loaded with cobalt ferrite ($CoFe_2O_4$)	84.98	150 Minutes	350 mg/L	0.05 g	4	–	23.14 mg/g	(Hoang et al., 2020)
RhB	Ni-Zn Fe_2O_4	98	30 Minutes	10 mg/L	0.5 g	–	30–37 °C	–	(Jadhav et al., 2020)
RhB	Nano iron oxide–modified biochar using Chlorella vulgaris (Cv)	–	180 Minutes	100 mg/L	30 mg	–	15–35 oC	286.4 mg/g	(Peng et al., 2022)
RhB	Mn-$ZnFe_2O_4$	82	90 Minutes	10 mg/L	3.2 g	4	–	34.5 mg/g	(Alharbi et al., 2023)
RhB	t-butyl phosphate- impregnated polymeric resin	98.45	30 Minutes	100 mg/L	0.3 g	3.6	–	43.47 mg/g	(Ali Khan et al., 2020)
RhB	$CoFe_2O_4$	90.6	270 Minutes	10 mg/L	0.1 g	–	–	–	(To Loan et al., 2019)
RhB	Amino acid functionalized Fe_3O_4 nanoparticles	70	30 Minutes	30 mg/L	50 mg	7	25 °C	10.44 mg/g	(Belachew et al., 2021)
RhB	$ZnNd_xFe_{2-x}O_4$	98	210 Minutes	10 mg/L	0.1 g	–	–	–	(Nguyen et al., 2021)
RhB	Graphite carbon/carbon nanotube composites	85	3 Hours	2.5–20 mg/L	0.6 g	3	20–60 °C	0.437 mg/g	(Zghal et al., 2023)
MB RhB	MgCF@SiO-NH-GA	99 98.2	30 Minutes	10 mg/L	50 mg	7	298 K	103 mg/g 89 mg/g	Current Study

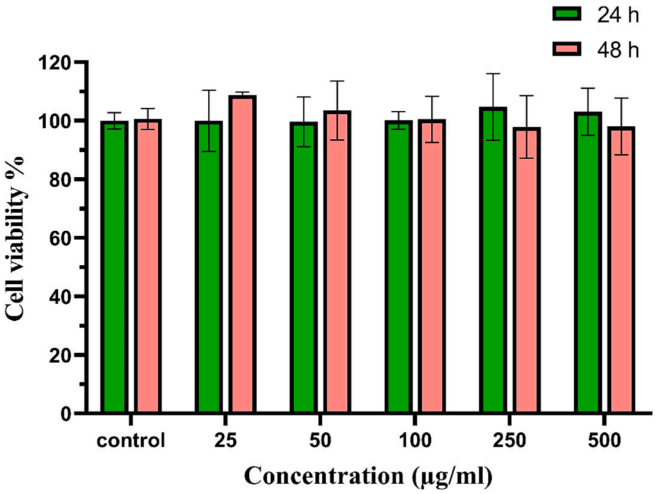

Fig. 13. Cell Viability test of MgCF@SiO–NH-GA nanoparticle.

adsorption tests for Methylene Blue and Rhodamine B dyes. The kinetic studies followed the Boyd kinetic model, whereas our experimental data was most accurately described by the Langmuir isotherm model. This revealed maximum adsorption capacities of 103 $mg.g^{-1}$ and 89 $mg.g^{-1}$ for MB and RhB, respectively. In addition, the MgCF-SiO_2-APTES-GA nanocomposite demonstrated high recyclability while maintaining adsorption–desorption efficacy for up to five cycles. This research offers not only a cost-effective solution but also a significant contribution to addressing the pressing environmental concerns tied to organic dye removal from wastewater.

Declaration of competing interest

The authors declare that they have no known competing financial interests or personal relationships that could have appeared to influence the work reported in this paper.

Appendix A. Supplementary data

Supplementary data to this article can be found online at https://doi.org/10.1016/j.arabjc.2024.105647.

References

Akpomie, K.G., Conradie, J., Adegoke, K.A., et al., 2023. Adsorption mechanism and modeling of radionuclides and heavy metals onto ZnO nanoparticles: a review. Appl Water Sci 13, 20.

Alharbi, A.F., Alotaibi, A.A., Gomaa, H.E., et al., 2023. Magnetic Biochar by One-Step Impregnation Pyrolysis of Peganum harmala L. for Removal of Rhodamine B. Adsorp. Sci. Technol. 2023.

Ali Khan, M., Momina, M.R., Siddiqui, et al., 2020. Removal of rhodamine b from water using a solvent impregnated polymeric dowex 5wx8 resin: Statistical optimization and batch adsorption studies. Polymers 12, 500.

Ali, N., Said, A., Ali, F., et al., 2020. Photocatalytic degradation of congo red dye from aqueous environment using cobalt ferrite nanostructures: development, characterization, and photocatalytic performance. Water Air Soil Pollut. 231, 1–16.

Bektar, M., Rasekh, H.A., Soltanianfard, M. J., 2020. Synthesis and characterization of CoFe2O4@ SiO2-polyethyleneimine magnetic nanoparticle and its application for ultrasonic-assisted removal of disulfine blue dye from aqueous solution 13, 5430-5437.

Belachew, N., Tadesse, A., Kahsay, M.H., et al., 2021. Synthesis of amino acid functionalized Fe 3 O 4 nanoparticles for adsorptive removal of Rhodamine B. Appl Water Sci 11, 1–9.

Daniel, L.S., Rahman, A., Hamushembe, M.N., et al., 2023. The production of activated carbon from Acacia erioloba seedpods via phosphoric acid activation method for the removal of methylene blue from water. Bioresource Technology Reports. 23, 101568.

Dănilă, R.-Ş., Dumitru, I., Ignat, M., et al., 2023. CoFe2O4@HaP as Magnetic Heterostructures for Sustainable Wastewater Treatment. 16, 2594.

Doan, L., 2023. Surface Modifications of Superparamagnetic Iron Oxide Nanoparticles with Polyvinyl Alcohol and Graphite as Methylene Blue Adsorbents. Coatings 13, 1558.

Eltaweil, A.S., Abd El-Monaem, E.M., El-Subruiti, G.M., et al., 2023. Graphene oxide incorporated cellulose acetate beads for efficient removal of methylene blue dye; isotherms, kinetic, mechanism and co-existing ions studies. J. Porous Mater. 30, 607–618.

Hoang, L.P., Van, H.T., Nguyen, T.T.H., et al., 2020. Coconut shell activated carbon/ CoFe2O4 composite for the removal of rhodamine B from aqueous solution. J. Chem. 2020, 1–12.

Iqbal, Z., Tanweer, M.S., Alam, M., 2023. Reduced Graphene Oxide-Modified Spinel Cobalt Ferrite Nanocomposite: Synthesis, Characterization, and Its Superior Adsorption Performance for Dyes and Heavy Metals. ACS Omega 8, 6376–6390.

Jadhav, S.A., Somvanshi, S.B., Khedkar, M.V., et al., 2020. Magneto-structural and photocatalytic behavior of mixed Ni–Zn nano-spinel ferrites: visible light-enabled active photodegradation of rhodamine B. J. Mater. Sci. Mater. Electron. 31, 11352–11365.

Jasim, N.A., Ebrahim, S.E., Ammar, S.H., 2023. Fabrication of ZnxMn1-xFe2O4 metal ferrites for boosted Photocatalytic Degradation of Rhodamine-B Dye. Results in Optics. 100508.

Jyothi, M., Angadi, V.J., Kanakalakshmi, T., et al., 2019. Magnetic nanoparticles impregnated, cross-linked, porous chitosan microspheres for efficient adsorption of methylene blue from pharmaceutical waste water. J. Polym. Environ. 27, 2408–2418.

Khalid, A., Ahmed, R., Taha, M., et al., 2023. Fe3O4 nanoparticles and Fe3O4@ SiO2 core-shell: synthesize, structural, morphological, linear, and nonlinear optical properties. Journal of Alloys.

Li, M., Fang, Q., Lai, Y., et al., 2023. CdS Nanoparticles Supported by Cobalt@ Carbon-Derived MOFs for the Improved Adsorption and Photodegradation of Ciprofloxacin. Int. J. Mol. Sci. 24, 11383.

Mund, H., Ahuja, B., 2017. Structural and magnetic properties of Mg doped cobalt ferrite nano particles prepared by sol-gel method. Mater. Res. Bull. 85, 228–233.

Nasiri, A., Rajabi, S., Hashemi, M., 2022. CoFe2O4@Methylcellulose/AC as a New, Green, and Eco-friendly Nano-magnetic adsorbent for removal of Reactive Red 198 from aqueous solution. Arabian J. Chem. 15, 103745. https://doi.org/10.1016/j.arabjc.2022.103745.

Nasrollahi, Z., Ebrahimian Pirbazari, A., Hasan-Zadeh, A., et al., 2019. One-pot hydrothermal synthesis and characterization of magnetic nanocomposite of titania-deposited copper ferrite/ferrite oxide for photocatalytic decomposition of methylene blue dye. International Nano Letters. 9, 327–338.

Nguyen, L.T., Nguyen, H.T., Le, T.H., et al., 2021. Enhanced photocatalytic activity of spherical Nd3+ substituted ZnFe2O4 nanoparticles. Materials. 14, 2054.

Peng, Z., Fan, Z., Chen, X., et al., 2022. Fabrication of nano iron oxide–modified biochar from co-hydrothermal carbonization of microalgae and Fe (II) salt for efficient removal of rhodamine B. Nanomaterials 12, 2271.

Rani, M., Murtaza, M., Amjad, A., et al., 2023. NiSe2/Ag3PO4 Nanocomposites for Enhanced Visible Light Photocatalysts for. Environmental Remediation Applications. 13, 929.

Rashdan, S.A., Hazeem, L.J., 2020. Synthesis of spinel ferrites nanoparticles and investigating their effect on the growth of microalgae Picochlorum sp. Arab Journal of Basic and Applied Sciences. 27, 134–141.

Salih, S.J., Kareem, A.S.A., Anwer, S.S., 2022. Adsorption of anionic dyes from textile wastewater utilizing raw corncob. Heliyon. 8.

Salih, S.J., Mahmood, W.M., 2023. Review on magnetic spinel ferrite (MFe2O4) nanoparticles: From synthesis to application. Heliyon.

Shojaei, S., Rahmani, M., Khajeh, M., et al., 2023. Ultrasound assisted based solid phase extraction for the preconcentration and spectrophotometric determination of malachite green and methylene blue in water samples. Arab. J. Chem. 16, 104868.

Suhaimi, N., Kooh, M.R.R., Lim, C.M., et al., 2022. The use of gigantochloa bamboo-derived biochar for the removal of methylene blue from aqueous solution. Adsorpt. Sci. Technol. 2022, 1–12.

Tara, N., Abomuti, M.A., Alshareef, F., et al., 2023. Nigella sativa-Manganese Ferrite-Reduced Graphene Oxide-Based Nanomaterial: A Novel Adsorbent for Water Treatment. Molecules 28, 5007.

Thy, L.T.M., Kiem, N.H., Tu, T.H., et al., 2020. Fabrication of manganese ferrite/ graphene oxide nanocomposites for removal of nickel ions, methylene blue from water. Chem. Phys. 533, 110700.

To Loan, N.T., Hien Lan, N.T., Thuy Hang, N.T., et al., 2019. CoFe2O4 nanomaterials: effect of annealing temperature on characterization, magnetic, photocatalytic, and photo-fenton properties. Processes. 7, 885.

Zango, Z.U., Dennis, J.O., Aljameel, A., et al., 2022. Effective removal of methylene blue from simulated wastewater using ZnO-chitosan nanocomposites: optimization, kinetics, and isotherm studies. Molecules 27, 4746.

Zghal, S., Jedidi, I., Cretin, M., et al., 2023. Adsorptive removal of Rhodamine B dye using carbon graphite/cnt composites as adsorbents: Kinetics, isotherms and thermodynamic study. Materials. 16, 1015.